

Method for time-dependent simulations of viscoelastic flows: vortex shedding behind cylinder

Paulo J. Oliveira*

Departamento de Engenharia Electromecânica, Universidade da Beira Interior, 6201-001 Covilhã, Portugal

Received 1 June 2001; received in revised form 2 August 2001

Abstract

In this paper, a comprehensive description of a finite-volume method for the simulation of time-dependent viscoelastic flows is given. It is applied to simulate the flow of a particular type of elastic fluid, having constant viscosity, but shear-thinning relaxation time, as it passes around a circular cylinder, forming and shedding vortices along its wake. Careful attention is given to the accuracy of the method, which is second-order in both the spatial and the temporal discretisation. Frequency of vortex shedding is shown to be attenuated by elasticity of the fluid, while the size of the formation zone behind the cylinder is elongated. These results are in agreement with recent experimental observations, as are further results showing a reduction in the root mean square (rms) fluctuating velocities compared with Newtonian flow. Consideration is also given to the effects of Reynolds number, extensibility parameter in the constitutive model, and Deborah number. In all cases, an increase on those two latter parameters leads to a delay, or a strong hindrance, of shedding formation. The mean drag coefficient decays with the Reynolds number, but it is smaller for the viscoelastic fluid. © 2001 Elsevier Science B.V. All rights reserved.

Keywords: Time-dependent flows; Numerical method; Vortex shedding; Viscoelastic fluid

1. Introduction

Many apparently steady two-dimensional flows of viscoelastic fluids are prone to instabilities which manifest themselves as transition to either three-dimensional flows or time-dependent, chaotic or periodic, flows [1,2]. This occurs in many of the flow problems often used as test cases in developing numerical methods for computational rheology, such as flows through contractions, flows around spheres or cylinders, etc. For example, Oliveira and Pinho [3] were able to obtain steady solutions up to a Deborah number of ≈ 10 for the flow of an upper-convected Maxwell fluid through a four to one planar contraction, but surprisingly, similar simulations (same method, grid, etc. [4]) with a PTT fluid revealed the flow to be unsteady at $De \approx 5$, with periodic formation and detachment of lip vortices at the entrance

* Fax: +351-275-329972.

E-mail address: pjpo@ubi.pt (P.J. Oliveira).

to the small channel. Although the simulations in [4] are still under investigation, it is clear that there is a need to derive an accurate method to simulating time-dependent flows of viscoelastic fluids obeying constitutive equations of the differential type. Ideally, that method should be such that it gives the steady solution, if it exists, as the asymptotic result following a time marching approach, otherwise, it captures the time-dependent behaviour of the solution, for an intrinsically unsteady flow.

Although there are a number of FEM-based methods reported in the literature especially designed for the simulation of time-dependent viscoelastic flows they are, most often, applied to obtain the transient behaviour of the numerical solution of a flow which is ultimately steady. Since that transient behaviour is very sensitive to the exact initial conditions, it is very difficult to compare the predicted transient with experimental results and hence assessment of the method is hindered. An interesting split Lagrangian–Eulerian method for such transient flows was developed by Harlen et al. [5]; it was applied to study the transient part of the solution for the well-known problem of a sphere falling along a tube, with a blockage ratio of 2. This method is decoupled, with the velocity–pressure problem solved with a finite element method (FEM), and the constitutive equation (Oldroyd-B or FENE-CR) solved in a Lagrangian fashion after being transformed into a co-rotating frame. An important drawback is that the method is only first-order both in space and, more important, in time. That method has recently been applied to solve the transient start-up flow of the “pom–pom” fluid model through a planar contraction [6]. The idea of decomposing a flow problem into Eulerian/Lagrangian sub-problems has been followed by others, for example, Wapperom et al. [7] developed a backward-tracking Lagrangian particle method which was subsequently applied to study the transient flow of the “pom–pom” fluid in a constriction [8]. For integral constitutive equations, Rasmussen and Hassager have developed the Lagrangian integral method, for both two-dimensional [9] and three-dimensional [10] flows, which appears to be one of the few FEM schemes offering second-order accuracy in time, as demonstrated in the (numerical) start-up sphere-in-cylinder flow problem.

In the context of finite volume methods (FVM), there have been a few attempts to extend time-marching procedures, typically used to obtain steady-state solutions, to the calculation of really time-dependent flows, e.g. [11,12]. In both of these papers, the methods are only first-order in time, and in [12], it is also first-order in space. No applications to intrinsically time-dependent flows were reported in those works. Mixed FEM/FVM of the time-marching type have also been developed, mainly by Wapperom and Webster (see e.g. [13] and references therein), but have not been applied to actual time-dependent flow situations. So, it appears that numerical simulation of time-dependent viscoelastic flows with the finite volume method is still at an incipient stage, and one of the purposes of the present work is to describe and apply such a method. As a suitable test case we have chosen the flow around a circular cylinder, which is known to produce a time-dependent pattern of shedding vortices, both for Newtonian and viscoelastic fluids. In the latter case a number of interesting features, to be discussed below, is known to occur. A second purpose of the work is to investigate numerically the effects of fluid elasticity on the characteristics of vortex shedding, in order to assess whether the experimentally observed features can be reproduced by the simulations.

In this respect, there has been quite a few recent papers in which marked differences between vortex shedding resulting from Newtonian fluids or polymer solutions have been reported, mostly based on experimental observations. The choice of the problem of vortex shedding formation with dilute polymer solutions as a suitable test case for time-dependent numerical schemes was prompted by the reading of a very recent (2001) paper by Cadot [14] which shows, based on visualisation and velocity measurements (PIV), the remarkable effects induced by fluid elasticity. Coloured streaklines give a visual indication of those effects; the wavelength of the vortex street behind the cylinder becomes longer (so shedding frequency and Strouhal number are reduced); the concentration of vorticity is weaker (partial roll-up;

vortex inhibition); the braids between vortices are strengthened; the formation region behind the cylinder is elongated (elasticity suppresses shear instability). Such effects are confirmed by other recent experimental sources [15–17] and, in fact, some were known for some time [18].

As far as we are aware there is no published systematic study of numerical predictions of vortex shedding with viscoelastic fluids, in the range of Reynolds numbers at which the wake remains basically two-dimensional and laminar (say $Re = 50$ – 150), and so we aimed the application of the proposed time-dependent numerical method to this problem. For lower Re , the flow remains steady (except for possible purely elastic instabilities at very low Re [1]), with a growing recirculation zone attached to the back of the cylinder, and a few numerical studies were devoted to this case ([19] with FEM; [20] with FVM). In these studies, the upper-convected Maxwell model was employed and the motivation was to explain the early experimental observations of James and Acosta [21], who found that beyond a critical Re the Nusselt number and drag coefficient C_D became independent of the approaching fluid velocity. It is interesting to note, in advance to presenting our results, that C_D in this situation of steady flow ($Re < 50$) is higher for the viscoelastic fluid (the elastic stretching of streamlines away from the cylinder makes this appear as if it had a larger diameter), but when the two-dimensional instability sets in and the flow becomes unsteady ($Re \gtrsim 50$), C_D for the viscoelastic fluid falls below the corresponding value for the Newtonian fluid at the same Re . We have, thus, a manifestation of “drag reducing” characteristic brought about by fluid elasticity. In conclusion, it may be considered that the present numerical results extend the results for the flow around a cylinder of Hu and Joseph [20] to higher Re , in the range where the flow becomes time periodic with vortex shedding. It is a challenge to see if simple differential constitutive models, appropriate for dilute polymer solutions and based on kinetic theory for finite-extensible dumbbell units, are able to qualitatively predict the experimental observations alluded above.

2. Equations

In this work, we will be concerned with polymer solutions obtained by dissolving a high-molecular polymer in a liquid solvent and, for the relatively low velocities and pressure found in vortex shedding experiments, the flow is incompressible, so the governing equations are

$$\nabla \cdot \mathbf{u} = 0, \quad (1)$$

$$\frac{\partial \rho \mathbf{u}}{\partial t} + \nabla \cdot (\rho \mathbf{u} \mathbf{u}) = -\nabla p + \nabla \cdot \boldsymbol{\tau}_s + \nabla \cdot \boldsymbol{\tau}, \quad (2)$$

expressing conservation of mass and momentum. In these equations, ρ , \mathbf{u} and p are the fluid density, velocity and pressure, $\boldsymbol{\tau}_s$ the solvent stress given by a Newtonian law $\boldsymbol{\tau}_s = 2\eta_s \mathbf{D}$ where η_s is the constant solvent viscosity and $\mathbf{D} = (\nabla \mathbf{u} + \nabla \mathbf{u}^T)/2$, and finally the polymer stress $\boldsymbol{\tau}$ must be obtained from an additional constitutive equation. At this point we could have chosen the well-known Oldroyd-B model, since one objective of the work is to develop the numerical method, but that model is known to be inadequate to represent dilute polymer solutions as it cannot predict the shear-thinning in the primary normal stress found in most of these fluids. For this reason we prefer to consider the molecular-based FENE family of models, developed from kinetic theory by Bird et al. [22], in which the stress is related to a conformation tensor \mathbf{A} by

$$\boldsymbol{\tau} = \frac{\eta_p f(\mathbf{A})}{\lambda} (\mathbf{A} - g(\mathbf{A})\mathbf{I}) \quad (3)$$

and \mathbf{A} evolves according to the hyperbolic equation:

$$\overset{\nabla}{\mathbf{A}} = -\frac{f(\mathbf{A})}{\lambda}(\mathbf{A} - g(\mathbf{A})\mathbf{I}), \quad (4)$$

where ∇ denotes the upper convected derivative, λ is the relaxation time (constant) and η_p the polymer-related viscosity (constant). The functions $f(\mathbf{A})$ and $g(\mathbf{A})$ in Eq. (3) depend on invariants of \mathbf{A} and represent, respectively, the strength of the spring in the molecular model and the effect of shear-thinning in viscosity. For a constant viscosity fluid with infinite spring extensibility we have $f = g = 1$ and it is easy to show that the usual equation for the Oldroyd-B model is recovered. For a fluid with finite spring extensibility the Peterlin approximation for f is often called for, giving $f = L^2/(L^2 - \text{Tr}(\mathbf{A}))$, and in this case the condition of constant viscosity ($g = 1$) yields the FENE-CR model [23]. If in addition, and for a question of simplicity, we make a further simplification:

$$\frac{Df(\mathbf{A})}{Dt} \approx 0, \quad (5)$$

then we obtain an implicit equation for $\boldsymbol{\tau}$:

$$\boldsymbol{\tau} + \frac{\lambda}{f(\boldsymbol{\tau})} \overset{\nabla}{\boldsymbol{\tau}} = 2\eta_p \mathbf{D}, \quad \text{with } f(\boldsymbol{\tau}) = \frac{L^2 + (\lambda/\eta_p)\text{Tr}(\boldsymbol{\tau})}{L^2 - 3}, \quad (6)$$

which allows us to work directly with $\boldsymbol{\tau}$, without resorting to the tensor \mathbf{A} . This model was used by Coates et al. [24] who referred to it as the modified Chilcott–Rallison model and have also presented its viscometric and elongational properties. In simple steady flows, the rheology is identical to that of the original Chilcott–Rallison fluid model, and therefore, we expect the present results to represent closely the flow of such a fluid. Clearly, if an effective relaxation time is defined as $\lambda(\dot{\gamma}) \equiv \lambda/f(\text{Tr}(\boldsymbol{\tau}))$, we see that $\lambda(\dot{\gamma})$ decreases with $\text{Tr}(\boldsymbol{\tau})$ increasing, thus, the model will be shear-thinning in the first normal stress difference. When the extensibility parameter L^2 (representing the ratio of the fully extended to the equilibrium size of the molecule) tends to infinity, $\lambda(\dot{\gamma}) \rightarrow \lambda$ and the Oldroyd-B model reappears.

Eq. (6) is the rheological constitutive equation used in the present study. It is straightforward to show (see also [24]) that the material functions in simple shear are identical to those of the original FENE-CR [23] and so studies with this latter model, and with the related FENE-P model, can be used as a guide in choosing the material parameter L^2 . While early works tended to use high values, of the order $\sim 10^3$ – 10^4 ([24], see discussion in [25]), there are arguments for using much lower values (~ 10) for Boger fluids [25,26], especially when the polymer concentration is high. Following the recent numerical study of Remmelgas et al. [27], we have decided to take $L^2 = 100$ as a base value, and later check its effect upon the calculations within the range 10^2 to 10^3 (100–1200), which covers most of the L^2 values used in the literature. For the flow around and past a cylinder, natural length and velocity scales are given by the cylinder diameter d and the unperturbed far-away velocity U . Time is then scaled with d/U and Reynolds and Deborah numbers are defined in the usual way, $Re = \rho U d / \eta$ and $De = \lambda U / d$, where the viscosity of the solution is given by $\eta \equiv \eta_s + \eta_p$. The only parameter left to define is the ratio between polymer and solvent viscosities. In studies with the FENE-CR this is usually given as a concentration parameter $c \equiv \eta_p / \eta_s$ which typically takes values of 0.1 for dilute solutions (e.g. [27]). Of course this value should be chosen according to the fluid that one intends to model, but it is important to realise that low values of c are to be expected when the concentration of the polymer in the solution is of a few 10–100 ppm. If we denote this volumetric concentration by x , then, we have $\eta = x\eta'_p + (1 - x)\eta'_s = \eta_p + \eta_s$ where η'

represents intrinsic viscosities. With $x \sim 10^{-5}$, we have $\eta'_s \approx \eta_s$ and $x\eta'_p = \eta_p$, and so η_p will be small compared with η_s . The retardation ratio $\beta \equiv \eta_s/\eta$ can be related to c by $\beta = 1/(1 + c)$, and a value of $c = 0.1$ gives a proportion of 9.1% for the polymer contribution to the total viscosity.

3. Numerical method

A fully implicit FVM is used, with non-orthogonal meshes (in general) and the collocated variable arrangement [28]. The governing equations (Eqs. (2) and (6)) are integrated in space over the control volumes (cells) forming the computational mesh, and in time over a time step (δt), so that sets of linearised algebraic equations are obtained, having the general form:

$$a_P \mathbf{u}_P = \sum_{F=1}^6 a_F \mathbf{u}_F + S_u, \quad (7)$$

to be solved for the velocity components, and

$$a_P^\tau \boldsymbol{\tau}_P = \sum_{F=1}^6 a_F^\tau \boldsymbol{\tau}_F + S_\tau, \quad (8)$$

to be solved for the stress components. In these equations a_F are coefficients, accounting for convection and diffusion influences, S are source terms encompassing all terms not included in the coefficients, the index P denotes the cell in question and F its neighbour cells. The mesh is structured by blocks and the cells are hexahedral, so in a general three-dimensional application F varies from 1 to 6; the dependent variables (\mathbf{u} , p and $\boldsymbol{\tau}$) are stored at the centre of the cells (collocated arrangement). The continuity Eq. (1) is also discretised resulting in a net balance of convection fluxes through the cell faces, and this constraint is used to obtain a pressure correction equation. Eqs. (7) and (8) can be viewed under the matrix form $Ax = b$ for linear equation systems, and are solved by a bi-conjugate gradient solver. Details of all this were given in a previous work [28] and so we can concentrate here on the changes introduced by the time-dependent nature of the present method. Two relevant modifications are in order: (1) the time-dependent terms in the governing equations need to be represented by a second-order scheme; and (2) the solution algorithm needs adjustment (iteration within a time step is required). These issues are discussed below.

Amongst the different options to achieve second-order accuracy in time (see e.g. [29]) we decided to use a second-order backward difference scheme (2BS) for the time derivatives (Φ is any variable):

$$\frac{\partial \Phi}{\partial t} \approx \frac{(1 + \kappa)\Phi^{n+1} - (1 + 2\kappa)\Phi^n + \kappa\Phi^{n-1}}{\delta t}, \quad (9)$$

where the parameter κ controls the scheme. If $\kappa = 0.5$, we have the 2BS with error $O(\delta t^2)$; with $\kappa = 0$, we have the implicit Euler scheme with error $O(\delta t)$. The 2BS is of straightforward implementation in the existing “time-marching” method; it has the drawback of requiring additional storage of the dependent variables at the previous time levels Φ^n and Φ^{n-1} . That extra storage is the same as that required by, for example, a Crank–Nicolson scheme, which is also second-order (with better error constant), but is of more complex implementation into the existing method. A minor drawback of the 2BS is that the cell face fluxes cannot be formulated, without introducing too much complexity, in such a way that they will be independent of the time step used in the calculations. For time-dependent flows this is not problematic

and the error introduced can be viewed as a truncation error in time; the results to be presented show that this error is negligible.

A description of the algorithm is facilitated by using a semi-discrete form of the equations. In this way, it becomes clearer at which level the different variables and terms are updated. We assume that the solution is known at time level t^n and we want to advance it to t^{n+1} . The algorithm is conveniently subdivided into two steps: the objective of the first is to obtain a velocity field which satisfies simultaneously a form of the momentum equations and the continuity equation; in the second, the stress is calculated, based on existing kinematics. We start then with the momentum Eq. (2). As mentioned above, the net efflux from cell P of convection and diffusion fluxes is represented with the coefficients, thus,

$$\nabla \cdot (\rho \mathbf{u} \mathbf{u} - \eta \nabla \cdot \mathbf{u}) \approx \sum_F a_F (\mathbf{u}_P - \mathbf{u}_F) = a_0 \mathbf{u}_P - \sum_F a_F \mathbf{u}_F \quad (10)$$

with $a_0 \equiv \sum_F a_F$. The semi-discrete forms of the momentum and continuity equations to be solved are then

$$\left(a_0 + (1 + \kappa) \frac{\rho V}{\delta t} \right) \mathbf{u}_P^{**} - \sum_F a_F \mathbf{u}_F^{**} = -\nabla p^* + \nabla \cdot \boldsymbol{\tau}^* + S'_u(\mathbf{u}^*) + \frac{\rho V}{\delta t} ((1 + 2\kappa) \mathbf{u}^n - \kappa \mathbf{u}^{n-1}), \quad (11)$$

$$\nabla \cdot \mathbf{u}^{n+1} = 0, \quad (12)$$

where V is the cell volume and S'_u represents additional source terms. Intermediate calculation levels within a time step are marked with asterisks. Thus, in Eq. (11), the convection and diffusion terms represented by the coefficients are treated implicitly when the equation is solved as a matrix equation for \mathbf{u}^{**} by means of a biconjugate-gradient solver. Pressure is treated in a semi-implicit way, as described below, and the stress divergence is evaluated explicitly (in the first iteration within a time step, p^* and $\boldsymbol{\tau}^*$ are assigned previous time-level values, p^n and $\boldsymbol{\tau}^n$). The equation set (11) and (12) represents the pressure–velocity problem, which results in a Poisson equation for the pressure correction ($p' \equiv p^{n+1} - p^*$) after writing a factorised-step momentum equation as

$$\begin{aligned} a_0 \mathbf{u}_P^{**} + (1 + \kappa) \frac{\rho V}{\delta t} \mathbf{u}_P^{n+1} - \sum_F a_F \mathbf{u}_F^{**} \\ = -\nabla p^{n+1} + \nabla \cdot \boldsymbol{\tau}^* + S'_u(\mathbf{u}^*) + \frac{\rho V}{\delta t} ((1 + 2\kappa) \mathbf{u}^n - \kappa \mathbf{u}^{n-1}), \end{aligned} \quad (13)$$

and subtracting it from Eq. (11) to obtain

$$(1 + \kappa) \frac{\rho V}{\delta t} (\mathbf{u}_P^{n+1} - \mathbf{u}_P^{**}) = -\nabla (p^{n+1} - p^*) = -\nabla p'. \quad (14)$$

Since \mathbf{u}^{n+1} is forced to satisfy continuity (cf. Eq. (12)), application of the divergence operator to this last equation yields the pressure correction equation:

$$\nabla \cdot \mathbf{u}^{**} = \nabla \cdot \frac{1}{(1 + \kappa)(\rho V / \delta t)} \nabla p'. \quad (15)$$

The matrix equation representing (15) is positive definite and is solved for p' with a symmetric conjugate gradient method as explained in [28]. Once p' is obtained, new time level values of pressure and velocity

are calculated from

$$p^{n+1} = p^* + p', \quad (16)$$

$$\mathbf{u}^{n+1} = \mathbf{u}^{**} - \frac{1}{(1 + \kappa)(\rho V / \delta t)} \nabla p', \quad (17)$$

where the last relation results from Eq. (14). We note that there is no need for any under-relaxation factor in this updating process.

At this stage the pressure–velocity problem within the present time step is solved, and we can proceed to the constitutive equation. Again, the time-dependent term in Eq. (6) is represented by the second-order 2BS scheme and the implicit equation to be solved for $\boldsymbol{\tau}$ is

$$\begin{aligned} \boldsymbol{\tau}^{n+1} + \frac{\lambda}{f(\boldsymbol{\tau}^*)} \left[\frac{(1 + \kappa)\boldsymbol{\tau}^{n+1} - (1 + 2\kappa)\boldsymbol{\tau}^n + \kappa\boldsymbol{\tau}^{n-1}}{\delta t} + \nabla \cdot \mathbf{u}^{n+1} \boldsymbol{\tau}^{n+1} \right] \\ = \eta_p (\nabla \mathbf{u}^{n+1} + \nabla \mathbf{u}^{Tn+1}) + \frac{\lambda}{f(\boldsymbol{\tau}^*)} (\boldsymbol{\tau}^* \cdot \nabla \mathbf{u}^{n+1} + \nabla \mathbf{u}^{Tn+1} \cdot \boldsymbol{\tau}^*). \end{aligned} \quad (18)$$

Careful attention must be paid to the discretisation of the convective term as a straightforward representation with the upwind scheme simply leads to too much numerical diffusion, but some degree of upwinding is required to retain the hyperbolic nature of the equation.

In this study, a special version of the second-order accurate, high resolution, SMART scheme [30] was applied; details of this will be given in a forthcoming publication [31]. A demonstration of the benefits brought about by high-resolution schemes (HRS) into viscoelastic flow computations can be found in [32] which also explains the deferred correction procedure used to incorporate HRS in standard FVM. Basically, the convection term is written as

$$\frac{\lambda}{f(\boldsymbol{\tau}^*)} \nabla \cdot \mathbf{u}^{n+1} \boldsymbol{\tau}^{n+1} \approx \sum_F a_F^\tau (\boldsymbol{\tau}_P^{n+1} - \boldsymbol{\tau}_F^{n+1}) \equiv a_0^\tau \boldsymbol{\tau}_P^{n+1} - \sum_F a_F^\tau \boldsymbol{\tau}_F^{n+1},$$

where the coefficients a_F^τ contain convection fluxes calculated with the upwind scheme, and a corrective term accounting for the HRS is introduced as a source term. The matrix form of the constitutive equation is then

$$\begin{aligned} \left[V + a_0^\tau + (1 + \kappa) \frac{\lambda V}{f(\boldsymbol{\tau}^*) \delta t} \right] \boldsymbol{\tau}_P^{n+1} - \sum_F a_F^\tau \boldsymbol{\tau}_F^{n+1} \\ = S_\tau(\mathbf{u}^{n+1}, \boldsymbol{\tau}^*) + S_{\tau\text{-HRS}} + \frac{\lambda V}{f(\boldsymbol{\tau}^*) \delta t} ((1 + 2\kappa)\boldsymbol{\tau}^n - \kappa\boldsymbol{\tau}^{n-1}), \end{aligned} \quad (19)$$

where $S_\tau(\mathbf{u}, \boldsymbol{\tau})$ includes the terms on the RHS of Eq. (18), and $S_{\tau\text{-HRS}}$ includes the HRS-related terms (see [32]).

At this stage we have both the velocity and the stress at the new time level, \mathbf{u}^{n+1} and $\boldsymbol{\tau}^{n+1}$. This algorithm, however, would be only first-order accurate (in time) because of the two following points:

1. In the pressure–velocity problem, we have introduced the approximated momentum Eq. (13) in order to be able to derive a manageable form for the pressure correction equation (this is equivalent to neglecting the convection/diffusion effects during the pressure update stage of the algorithm).

2. Stress and velocity have been decoupled, that is, \mathbf{u}^{n+1} was based on the old-time level stress ($\boldsymbol{\tau}^* = \boldsymbol{\tau}^n$).

An effective way to overcome these problems is to iterate through Eqs. (11), (15)–(17) and (19); that is, \mathbf{u}^{n+1} and $\boldsymbol{\tau}^{n+1}$ are viewed only as approximated values to the new time fields, are written as \mathbf{u}^* and $\boldsymbol{\tau}^*$, and the algorithm is repeated until a convergence criterion is achieved. In most of the calculations to be reported, the maximum normalised residuals of all equations (evaluated as the L_1 norm) had to fall below 1% for iterative convergence within a time step. Depending on the value of the time step, the number of iterations typically varied between 3 and 5; when the flow conditions were not fully developed in time, for example in the first time steps when restarting from a field at a lower De number, the number of iterations tended to increase but, quickly after, would fall to constant values of the order given above.

In the present implementation, the coefficients and source terms (a_F , S) were recalculated at every iteration, so that the scheme faithfully represents a fully implicit scheme. We believe, guided by the analysis given by Issa [33], that this is not a necessary requirement to guarantee second-order accuracy, and important computer time savings can be gained if the coefficients are stored and re-used. Of course, such time savings are realised at the expense of some additional storage memory. If this strategy is followed (a matter for future research), then at each time step we are faced with an “explicitly” linear problem, with algebraic linear equations to be solved for velocity and stress, and the stability of the procedure should be enhanced. In fact, it becomes similar to the application of a factored or operator-splitting procedure, such as PISO [33], when the number of correction stages is not fixed a priori, but is left to vary in order to meet a convergence criterion.

We want to emphasise the point that the algorithm just described is not standard, even for Newtonian calculations, in that it dispenses with the need to under-relax the equations at each time step. In a recent study, Barton [34] proposed a different approach for time-dependent problems with Newtonian fluids, where the under-relaxation factors varied within the time step in such a way that they became equal to one at the last iteration, so that the solution at the new time would not depend on the value used for those factors. We found that dispensing altogether with under-relaxation factors, by employing the present algorithm based on the corrector momentum Eq. (13), yields very significant gains: Newtonian runs starting from a rest state ($t = 0$), up to a fully developed shedding state (at $t = 200$), took twice as long in CPU time when the standard SIMPLE algorithm was used with under-relaxation factors of 0.8, as compared with the present algorithm. In absolute terms this represents a gain of a few hours of CPU. We note that all computations to be reported have been carried out in a portable PC running at 433 MHz.

4. Results

Results from application of the method described in Section 3 to the problem of vortex shedding from a circular cylinder are presented and discussed. The discussion is divided into two main parts, one dealing with the important question of accuracy of the temporal and spatial discretisation, and the other with the physical effects of elasticity on the flow. As a base case we take the Newtonian flow at a Reynolds number of 100, and then the relaxation time is gradually increased up to a Deborah number of 80, at a constant value of the extensibility parameter, $L^2 = 100$. The polymer concentration is assumed to be $c = 0.1$. At a later stage, we study the effect of varying the Reynolds number (from 50 to 120) and the extensibility parameter (from 100 to 1200).

Table 1
Characteristics of the various computational meshes

Grids	N_C	N_θ	δr_{\min}	δr_{\max}	δs_{\min}	L_H	L_V	f_r
Mesh-1	9600	160	0.02	2.3	0.02	60	60	1.0838
Mesh-2	38400	320	0.01	1.17	0.01	60	60	1.0410
Mesh-3	19860	180	0.02	0.477	0.02/0.0081 ^a	30 + 15	30	1.0326 ^b

^a On rear of cylinder (wake region).

^b Also uses $f_\theta = 1.0309$.

It will be shown that the second-order accuracy of both the temporal and the spatial discretisation schemes is an essential requirement to making realistic predictions. Furthermore, the present calculations exhibit many of the “elastic” effects observed in experiments: attenuation of vortex shedding frequency, reduction of the lift coefficient and delay of vortex formation.

4.1. Accuracy

4.1.1. Effect of mesh refinement

Three non-orthogonal computational meshes have been employed to discretise the flow domain around the cylinder, and their main characteristics are given in Table 1: total number of cells (N_C); number of cells around cylinder (N_θ); minimum and maximum cell spacing along the radial (δr_{\min} , δr_{\max}) and the tangential (δs_{\min}) directions (values are normalised with cylinder diameter d); size of the computation domain, in the main flow direction (horizontal, L_H) and the cross-stream direction (vertical, L_V); and finally, the geometrical expansion factor used to concentrate the mesh around the cylinder surface (f_r). This latter factor is important because it indicates the rate of increase of the cell size, for two adjacent cells, and it is necessary to keep it as low as possible to avoid degradation of the order of accuracy of the spatial discretisation schemes. A Cartesian frame of reference is centred at the cylinder axis (see Fig. 1), with x aligned with the undisturbed fluid velocity U . The two first meshes in Table 1 were designed to assess the effect of consistent mesh refinement, and Mesh-2 was obtained from Mesh-1 after doubling the number of cells in both directions, and using the square root of the expansion factors [35]. Mesh-3 was then designed so as to have identical resolution near the cylinder as Mesh-1, but providing much better resolution on the rear and the far wake regions of the cylinder (cf. the values of δr_{\max}); a portion of this mesh is shown in Fig. 1.

On the two first meshes the inlet plane is placed at $x = -30d$, the outlet plane at $x = +30d$, and two symmetry planes at $y = \pm 30d$. On Mesh-3, the lateral distance to the two symmetry planes was reduced to $y = \pm 15d$, as well as the distance to inlet, $x = -15d$, but the wake extended up to the same distance $x = +30d$. At the inlet plane a uniform streamwise velocity U was imposed and the stresses set to zero. At the outlet plane, streamwise gradients ($\partial/\partial x$) for all variables, including the pressure gradient, were set to zero. It has been checked that the position of both symmetry and outlet planes relatively to the cylinder did not introduced any appreciable distortion of the flow field.

The size of the computational domain was designed so that the simulations would represent the unbounded flow around a cylinder. When the lateral distance from the cylinder to the symmetry planes is too small, a blockage effect induces higher lift and drag coefficients, as compared to the unbounded case. The values $\pm 15d$ were found adequate by Lilek et al. [29] for Newtonian calculations, who quote an error $<0.5\%$ compared with simulations where the domain extended laterally to $\pm 25d$.

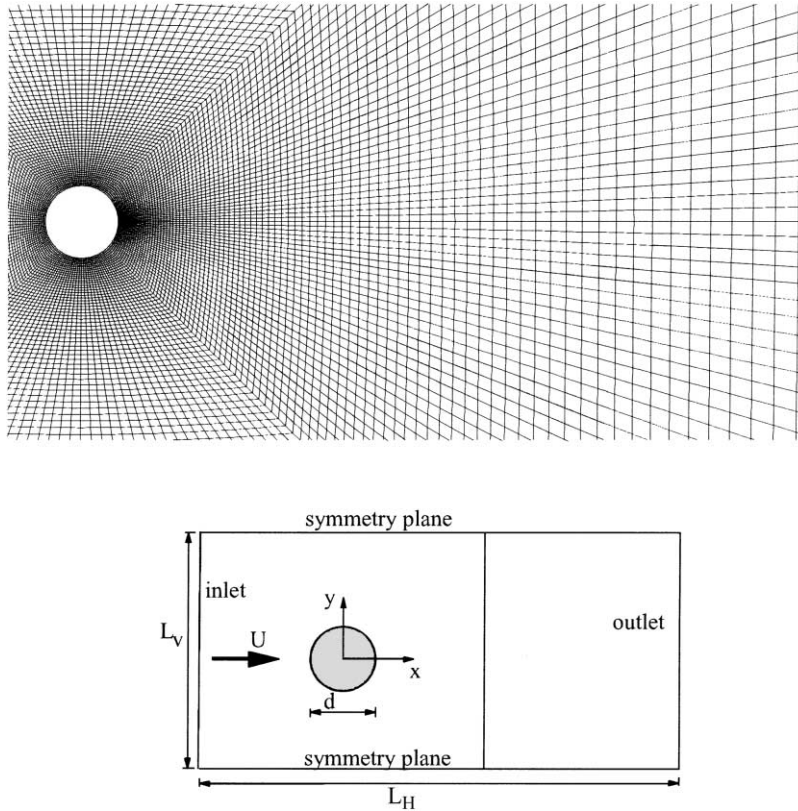


Fig. 1. Zoomed view of Mesh-3 (region, $x/d = -1$ to $+10$; $y/d = -3$ to $+3$) and sketch of flow domain (not to scale; in reality, $L_V/d = 60$ or 30).

For the base Newtonian case ($De = 0$, $Re = 100$) we obtained the values for the Strouhal number ($St \equiv f_S d/U$, $f_S =$ shedding frequency), and magnitude of lift and drag coefficients given in Table 2. The time-dependent drag and lift coefficients are defined by $C_D \equiv F_x/0.5\rho U^2 d$ and $C_L \equiv F_y/0.5\rho U^2 d$, where F_x and F_y are the components of the force on the cylinder, and the lift amplitude and mean drag are then calculated as $\Delta C_L = (C_{L_{\max}} - C_{L_{\min}})/2$ and $\bar{C}_D = 0.5(C_{D_{\max}} + C_{D_{\min}})$, respectively. In these runs the second-order spatial and temporal schemes have been employed, and the dimensionless time

Table 2
Mesh refinement results ($De = 0$, $Re = 100$)

	T_L	St	ΔC_L	$C_{D_{\max}}$	$C_{D_{\min}}$	\bar{C}_D
Mesh-1	5.9986	0.1667	0.3489	1.3704	1.3491	1.3598
Mesh-2	6.0303	0.1658	0.3321	1.3568	1.3376	1.3472
Mesh-3	5.9886	0.1670	0.3425	1.3800	1.3603	1.3701
Our extrapolation ^a	6.0409	0.1655	0.3265	1.3523	1.3338	1.3430
[29]	5.9916	0.1669	0.3400	1.3663	1.3469	1.3566

^a From Mesh-1 and -2.

step value was $\delta t = 0.05$ (recall the time units, d/U) which corresponds to 120 time steps for a period of the fluctuating lift force on the cylinder. Initial conditions for these runs were completely symmetric, basically corresponding to the situation of the fluid at rest, and the oscillatory flow was found to establish itself naturally, after an initial set-up time of about $t = 200$, after which the variation with time of C_L and C_D was seen to be perfectly sinusoidal (that will be seen in later figures). So it was an easy matter to extract from the graph C_L versus t the period of the oscillation, given in dimensionless terms by T_L , and the frequency of vortex shedding, $St = 1/T_L$. Those values, obtained on the three meshes, are given in Table 2 where the data from [29] are also given for comparison. That data were obtained from Richardson's extrapolation of the results of calculations on three consistently refined meshes, and so serves well the purpose of assessing the present results. It is seen that St on Mesh-1 or Mesh-3 is within 0.7% of the value on the fine mesh (this is a measurement of the accuracy of the present results). Values of ΔC_L and \bar{C}_D agree to within 0.7 and 1%, respectively, with those of [29]. The average \bar{C}_D of [29] is higher than ours on Mesh-2 and that might be an indication of the blockage induced error (Lilek et al., used $L_V = 32$). The same trend occurs for our \bar{C}_D on Mesh-3, but the difference is still rather small ($<1.7\%$).

We may, thus, conclude that the estimated accuracy of our results for the shedding frequency is $<1\%$ on Mesh-3 and so we shall use that mesh for the remaining calculations. The effect of the time step and discretisation scheme is now studied, with both Newtonian and viscoelastic flow cases.

4.1.2. Time discretisation

For the above Newtonian results the time step was $\delta t = 0.05$ and the second-order backward scheme was utilised to represent the time derivative terms. When the time step is halved to $\delta t = 0.025$, and then to $\delta t = 0.0125$, the results in terms of C_L and C_D are virtually unchanged, as shown in Fig. 2 and Table 3, for the base viscoelastic case ($De = 80$, $L^2 = 100$, $Re = 100$). Particularly in the figure the differences are so small that cannot be distinguished, a sign that the second-order scheme provides good time resolution even with a time step as large as 0.05, and so the discretisation errors are basically controlled by the spatial discretisation. However, when the first-order Euler scheme is used instead, as in many other works (e.g. [5–8,11,12]), the results in Fig. 2 and Table 3 show a considerable deterioration in precision. The numerical diffusion-like effect of the first-order Euler scheme produces a generalised reduction on the amplitude of the oscillations for both C_L and C_D , and that effect is felt even for a time step as low as $\delta t = 0.00625$ (reason why similarly low δt are used in other works, e.g. [34]). By allowing a time step as large as 0.05 (which, it is noted, corresponds to a maximum local Courant number of about ≈ 3 –6), but yet retaining good temporal accuracy, the 2BS scheme and the present fully implicit method provide an effective way of computing time-dependent flows in reasonable times.

Table 3
Effect of time-step with the second-order backward scheme (2BS) and the first-order Euler scheme

δt	2BS			Euler		
	ΔC_L	\bar{C}_D	$\Delta C_L (\times 10^{-2})$	ΔC_L	\bar{C}_D	$\Delta C_L (\times 10^{-2})$
0.05	0.1500	1.2962	0.17	0.0964	1.2592	0.145
0.025	0.1500	1.2966	0.175	0.1175	1.2746	0.075
0.0125	0.1501	1.2975	0.17	0.1311	1.2848	0.115
0.00625	–	–	–	0.1391	1.2910	0.135

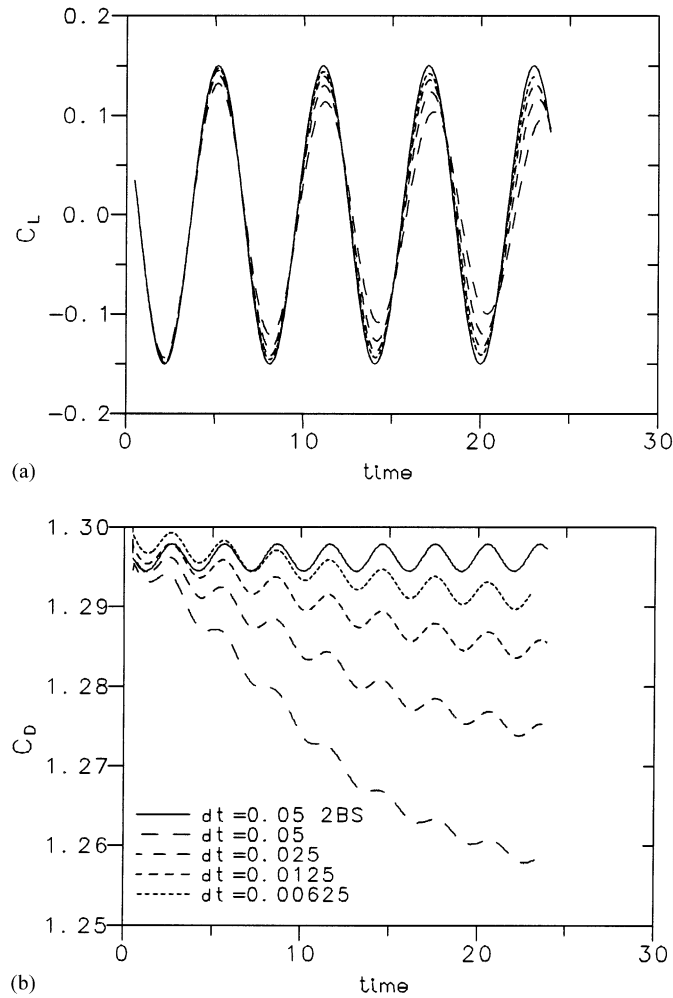


Fig. 2. Effect of time step size on the variation of (a) C_L and (b) C_D , using two time discretisation schemes: second-order backward (2BS) and Euler schemes (viscoelastic case, $De = 80$, $L^2 = 100$, $Re = 100$). Note that with 2BS, curves for the various δt coincide.

When the time step is too large, and when first-order time discretisation is coupled with first-order spatial discretisation, damping of the amplitude of the oscillations, and of the mean value of C_D as well, can be such that vortex shedding is suppressed altogether. This will be seen in the next results.

4.1.3. Spatial discretisation of convective terms

While the diffusive terms in the momentum equation, and the part of the Oldroyd derivative terms in the constitutive equation which is put into the source term of the corresponding algebraic equation, can be easily evaluated by means of second-order schemes simply by using linear interpolation in approximating the required cell face values, the same is not so simple for the convective terms. As base second-order schemes we have implemented the central-difference scheme (CDS), via deferred

correction, to represent the convective terms in the momentum equation, and the high-resolution also second-order accurate (at least) scheme, CUBISTA [31], to represent the convective terms in the constitutive equation. It is important to realise that accuracy higher than first-order is required in the momentum equation because the Reynolds number is high ($Re = 100$, in the base case), and in the constitutive equation when the Deborah number is also high ($De = 80$ in the base case, with $L^2 = 100$). When the upwind scheme (UDS) is employed for the convective terms in both equations, the results for the evolution of C_L and C_D are as represented in Fig. 3. Numerical diffusion becomes so strong that C_L is dampened from limiting values of ± 0.1500 to ± 0.0626 , C_D becomes higher, but without oscillations, and vortex shedding simply vanishes. These results, together with those of the previous subsection, provide clear and ineluctable evidence for the need to using high-order schemes (at least

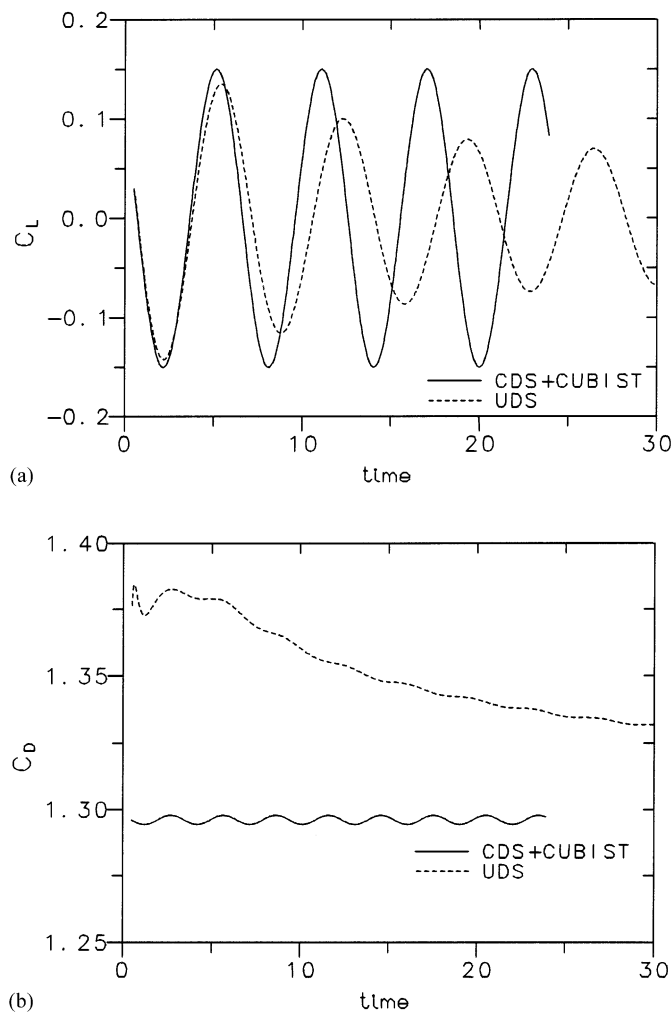


Fig. 3. Effect of spatial discretisation on the time variation of (a) C_L and (b) C_D (viscoelastic case, $De = 80$, $L^2 = 100$, $Re = 100$, $\delta t = 0.05$).

second-order) if accurate solutions are to be expected in viscoelastic flow simulations. In this particular flow case, it has been checked that vortex shedding behind the cylinder was again obtained when the convection terms in the momentum equation were discretised with central-differences, but those in the constitutive equation were still discretised with upwinding. Amplitude of C_L was however reduced by a large amount.

4.2. Physical results

4.2.1. Influence of elasticity (at $L^2 = 100$)

Experimental evidence has revealed [14–18] that even small amounts of a dissolved polymer, compared to the purely Newtonian solvent, lead to a reduction in frequency of vortex shedding, larger wavelength of the Karman street, increased length of the formation region just behind the cylinder, and alteration of the form of the relative vorticity patterns. These observations have been correlated with (or explained by) higher elongational viscosity of an elastic liquid and suppression of velocity fluctuations [17]. It is interesting to see if the numerical simulations are able to reproduce these trends, in spite of the simplicity of the constitutive model here employed.

Table 4 gives a summary of the main results obtained when elasticity is increased, by increasing De at a constant $Re = 100$ and $L^2 = 100$. We see that for this base case, as De goes from 0 to 80, the lift oscillation period is increased by 5.8% while the frequency measured by the Strouhal number is reduced in the same proportion. This effect is made clearer in Fig. 4, which shows the variation with time of the lift coefficient for the Newtonian case (curve with solid line) and the viscoelastic case, $De = 80$ (curve with dashed line). The time origin was chosen arbitrarily at a moment within the fully-developed oscillatory regime in which C_L reaches a minimum; both curves exhibit a perfectly sinusoidal behaviour, maintaining the period and amplitude. Not only is the frequency of the shedding in the viscoelastic flow case markedly lower compared with the Newtonian case, but also the amplitude of the lift coefficient. In fact, damping of maximum values of lift and drag by elasticity is stronger than damping in frequency, as shown by the plot of ΔC_L and ΔC_D versus De in Fig. 5. For a Deborah number larger than around

Table 4
Results for increasing Deborah number ($Re = 100$, $L^2 = 100$)

De	St	ΔC_L	\bar{C}_D	$\Delta C_D (\times 10^{-2})$	$C_{D_{\max}}$	$C_{D_{\min}}$	u'^a	v'^a
0	0.1670	0.3425	1.3701	0.985	1.3800	1.3603	0.0499	0.316
0.5	0.1659	0.3234	1.3795	0.900	1.3885	1.3705	0.0469	0.300
1.0	0.1644	0.2901	1.3732	0.735	1.3806	1.3659	0.0402	0.282
2.0	0.1620	0.2404	1.3527	0.510	1.3578	1.3476	0.0287	0.237
3.0	0.1605	0.2133	1.3386	0.400	1.3426	1.3346	0.0231	0.215
4.0	0.1597	0.1977	1.3296	0.345	1.3330	1.3261	0.0201	0.201
5.0	0.1591	0.1878	1.3235	0.310	1.3266	1.3204	0.0186	0.191
10	0.1579	0.1669	1.3098	0.235	1.3121	1.3074	0.0161	0.172
20	0.1575	0.1565	1.3022	0.195	1.3041	1.3002	0.0151	0.161
40	0.1576	0.1521	1.2983	0.180	1.3001	1.2965	0.0147	0.155
60	0.1577	0.1507	1.2970	0.175	1.2987	1.2952	0.0147	0.156
80	0.1578	0.1500	1.2962	0.170	1.2979	1.2945	0.0147	0.157

^a At $1d$ behind cylinder ($y = 0$); lateral velocity rms $v' = ((v - \bar{v})^2)^{1/2} / U$ (similarly for axial rms u').

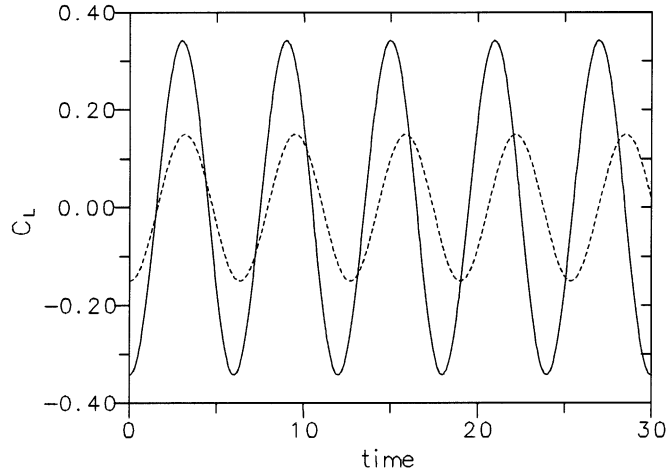


Fig. 4. Comparison of Newtonian (solid line) and viscoelastic ($De = 80$, dashed line) lift coefficient.

$De \approx 20$ – 30 , no further reduction in the lift and drag coefficients is observed. This may be explained by noting that the relaxation time of the fluid is then larger than the period of vortex shedding ($T_L \approx 6.35$) and the controlling time scale becomes the latter.

The relative difference between the Newtonian Strouhal number (St_N) and the viscoelastic Strouhal number (St_V) is shown in a log–log plot, as a function of elasticity (De), in Fig. 6. For comparison, the line expressing the average rate of decay passing through the experimental data of Usui et al. [18] ($St_N - St_V \sim De^{0.32}$) is also plotted. It should be recalled that the present predictions in Fig. 6 are for the modified FENE-CR model with a constant extensibility parameter $L^2 = 100$, whereas the data

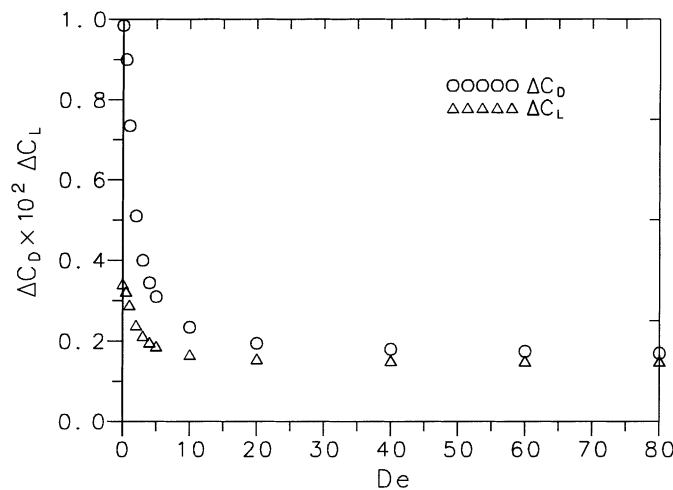


Fig. 5. Reduction of the amplitude of the drag and lift coefficients with elasticity ($L^2 = 100$).

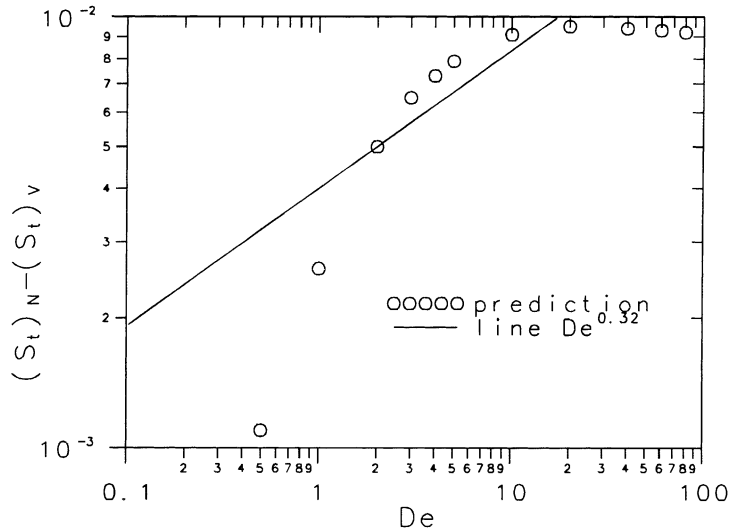


Fig. 6. Predicted difference between Newtonian and viscoelastic Strouhal numbers as a function of Deborah number ($L^2 = 100$). Comparison with rate-of-decrease curve $De^{0.32}$ given by Usui et al. [18].

given in Fig. 4 of Usui et al. [18] and fitted by the above curve correspond to a polyethylene oxide solution under different concentrations, and the relaxation time used to define De in that work was estimated in a rather arbitrary way. In any case it is interesting to see that the experimental rate of decay of the Strouhal number with De found by Usui et al. is very approximately followed by the present predictions in a decade or so of De . Considering that the experimental results of Usui et al. show some spread around the line fit they proposed, the comparison in Fig. 6 is encouraging, and in fact the deviation of the predictions from the fitted rate of decay is also seen in the experimental data (see Fig. 4 in [18]).

Streaklines for the base Newtonian and viscoelastic cases ($De = 0$ and 80) are shown in Fig. 7. These were obtained by tracking massless particles released every time step (here, $\delta t = 0.05$) from four positions very close to the upper side of the cylinder and four positions on the lower side. It is already apparent that the low-velocity formation region behind the cylinder is longer for the viscoelastic fluid and that, on the other hand, the vorticity of the Newtonian eddies detached from the cylinder is stronger (these vortices are more rolled-up). With increased elongational viscosity (by increasing L^2), those aspects of the vortical pattern are accentuated and will be further discussed below (Section 4.2.3).

4.2.2. Effect of Reynolds number

The Reynolds number was varied in the range $Re = 50$ – 120 , for both the Newtonian and the base viscoelastic cases ($De = 80$, $L^2 = 100$), and the resulting predictions in terms of St , C_L , C_D and \bar{X}_r (time average length of recirculation zone) are summarised in Table 5 and plotted in Figs. 8 and 9. In Fig. 8, our prediction of Strouhal number versus Re for the Newtonian case are compared with curve fits to experimental data proposed by Williamson [36] ($St = 0.1816 - 3.3265/Re + 1.6 \times 10^{-4}Re$) and by Roshko [37] ($St = 0.212 - 4.5/Re$), and also with the finite-volume numerical results of Lilek et al.

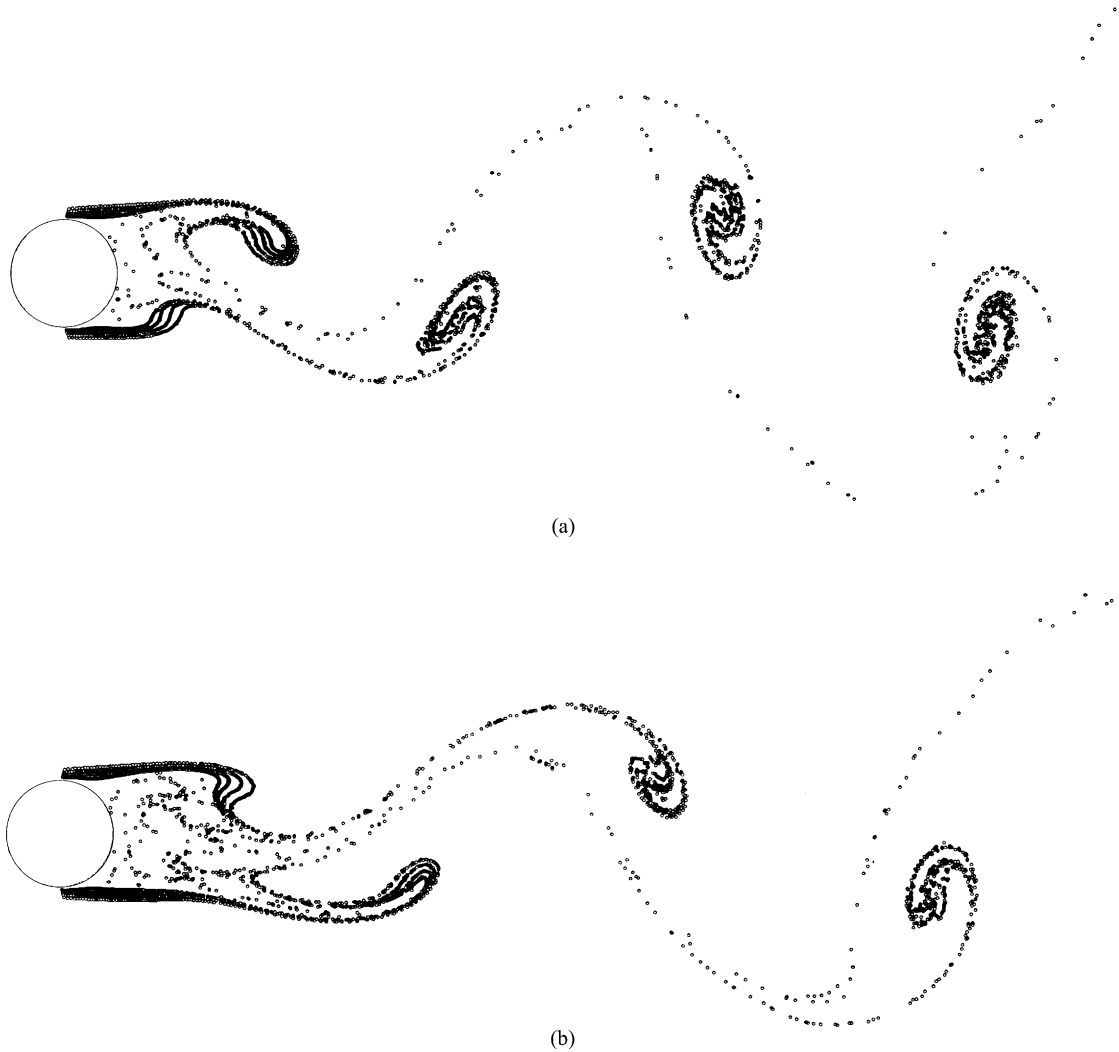


Fig. 7. Streaklines for the base Newtonian (a) and viscoelastic (b) cases.

[29]. Very good agreement is found with the predictions of [29] and the agreement is also good with Roshko fit. This quantitative agreement gives confidence on the correctness of the present method and its computer implementation. The viscoelastic data lie below the Newtonian, reflecting the tendency for vortex suppression induced by the elastic stresses, and of course in this case we do not have experimental or other data for comparison.

It is not only the frequency of vortex shedding which is reduced by elasticity effects, but even more strongly so the amplitude of the lift coefficient, as shown in Fig. 9a where we see a reduction to half of the $C_{L_{\max}}$ at $Re = 120$. The average drag accompanies that tendency and falls with Re (Fig. 9b), for both the Newtonian and viscoelastic cases, while being lower for the viscoelastic case, on account of the

Table 5

Results for increasing Reynolds number

Re	St	\bar{X}_r	ΔC_L	C_{Dmax}	C_{Dmin}	\bar{C}_D
Newtonian						
50	0.1261	2.393	0.0602	1.4764	1.4761	1.4762
60	0.1380	2.076	0.1360	1.4403	1.4382	1.4392
80	0.1552	1.644	0.2516	1.3998	1.3905	1.3952
100	0.1670	1.402	0.3425	1.3800	1.3603	1.3701
120	0.1757	1.229	0.4256	1.3741	1.3415	1.3578
Viscoelastic ($De = 80, L^2 = 100$)						
50	0.1217	2.826	≈ 0.0	1.4783	1.4783	1.4783
60	0.1288	2.969	0.0252	1.4010	1.4010	1.4010
80	0.1459	2.478	0.0901	1.3328	1.3317	1.3322
100	0.1578	2.065	0.1500	1.2979	1.2945	1.2962
120	0.1684	1.742	0.2106	1.2833	1.2756	1.2794

fact that the forming vortices remain attached for longer periods at the rear of the cylinder. For lower Re when the flow is steady, that trend is reversed: drag is higher for the viscoelastic fluid, as found by [19–21]. Numerical results not shown here confirm this trend which is already apparent from the C_D variation in Fig. 9b. A point worth noting in Fig. 9a is that, at $Re = 50$ vortex shedding is completely suppressed for the viscoelastic fluid ($\Delta C_L \approx 0$), while for the Newtonian fluid it is known that the vortex street is initiated at about $Re = 46$. This feature is reflected on the sudden variation of the average recirculation length (\bar{X}_r) behind the cylinder shown in Fig. 10. \bar{X}_r was computed as the time average over many shedding cycles of the x value along the centreline behind the cylinder ($y = 0$) at which u was zero. It is an interesting quantity in that it reveals how viscoelasticity tends to delay vortex formation by

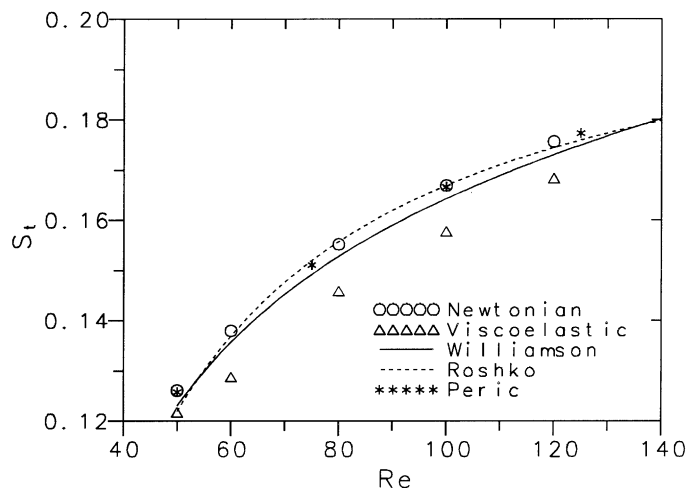


Fig. 8. Strouhal number vs. Reynolds number for the Newtonian and viscoelastic case ($De = 80, L^2 = 100$). Comparison with other sources.

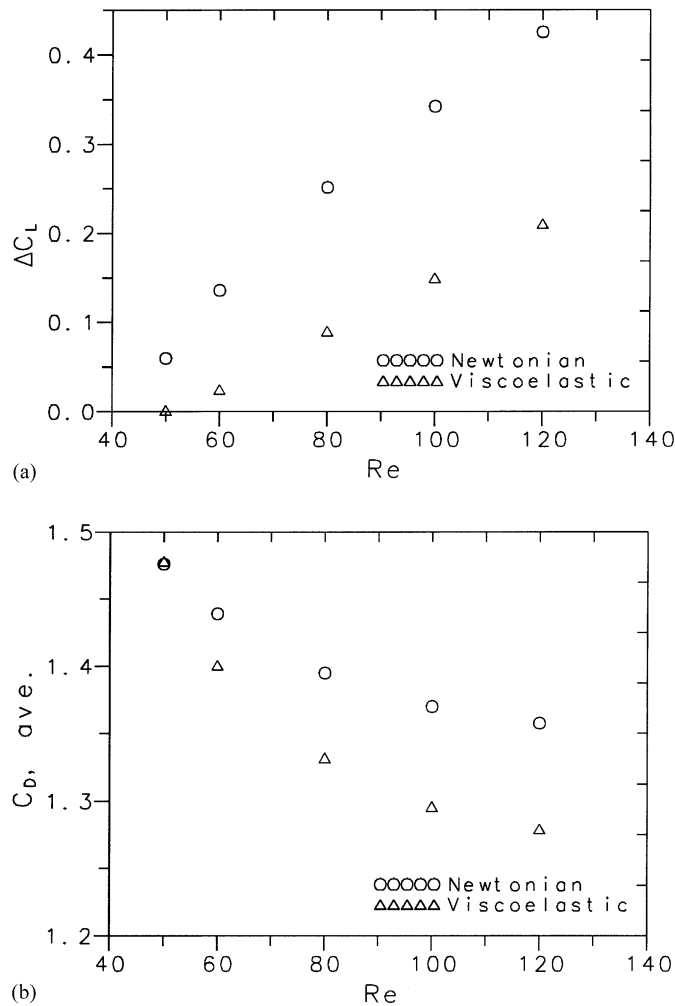


Fig. 9. Effect of Reynolds number on the (a) amplitude of lift, and (b) mean drag, for the Newtonian and viscoelastic case ($De = 80$, $L^2 = 100$).

extending the length of the formation zone behind the cylinder. Further evidence for this will be given in the next subsection where the formation zone is illustrated by means of streaklines. In Fig. 10, \bar{X}_r predictions of Kim and Choi [38] are also plotted for the purpose of comparison; they used an unstructured finite-volume method and, once more, our Newtonian results follow very well these independent data.

4.2.3. Effect of model parameter L^2

When the extensibility parameter L^2 is raised, the FENE model here employed predicts higher elongational viscosity in a uniaxial flow; if L^2 tends to infinity, then the model becomes the Oldroyd-B with a well-known singularity in the elongational viscosity at a finite stretch rate. It is common in the lit-

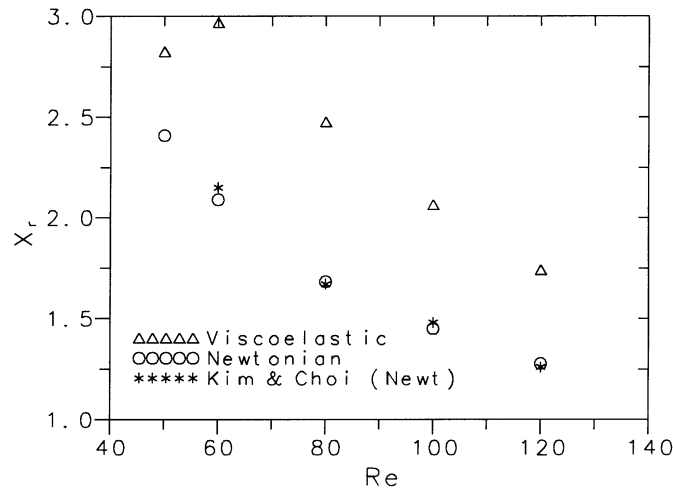


Fig. 10. Variation of the time mean length of the recirculation zone behind the cylinder with the Reynolds number, for the Newtonian and viscoelastic case ($De = 80$, $L^2 = 100$). Comparison with other sources.

erature to find applications of the FENE-CR with $L^2 = 100$ (or lower), e.g. [25], but values as high as ≈ 1200 are also found (e.g. [27]). The results of varying L^2 from 100 to 1200 at constant values of $De = 1$ and $Re = 100$ are given in Table 6. At this relatively low Deborah number, the trends are similar to those resulting from increased elasticity: the shedding period increases very slightly (by about 1.9%), so frequency is reduced as are the amplitude of the lift coefficient and the velocity fluctuations. A zoomed view of the instantaneous streamlines is shown in Fig. 11 where it is apparent that L^2 tends to increase and distort the formation zone behind the cylinder, features that may explain the slight rise of C_D seen in Table 6 as a consequence of a distorted pressure field around the cylinder.

What is more interesting is the effect of increased L^2 coupled with higher elasticity, as measured by De . For the highest tested value of $L^2 = 1200$, Table 7 gives a summary of the results obtained for $De = 1, 2$ and 3. For $De = 3.5$, we were not able to obtain converged results, even after lowering the time step to $\delta t = 0.00625$, and then to 0.003125. The shedding period is seen to increase by 11% (and the Strouhal number to decrease by the same margin), when De rises from 1 to 3, and this is accompanied

Table 6
Results for varying extensibility parameter L^2 ($De = 1$, $Re = 100$)

L^2	δt	T_L	St	ΔC_L	$C_{D_{\max}}$	$C_{D_{\min}}$	v'
100	0.05	6.0816	0.1644	0.2901	1.3806	1.3659	0.282
200	0.05	6.1150	0.1635	0.2790	1.3858	1.3721	0.267
300	0.05	6.1334	0.1630	0.2746	1.3903	1.3771	0.267
600	0.025	6.1643	0.1622	0.2673	1.4025	1.3897	0.263
900	0.025	6.1810	0.1618	0.2663	1.4133	1.4005	0.261
1200	0.025	6.1961	0.1614	0.2662	1.4221	1.4092	0.260

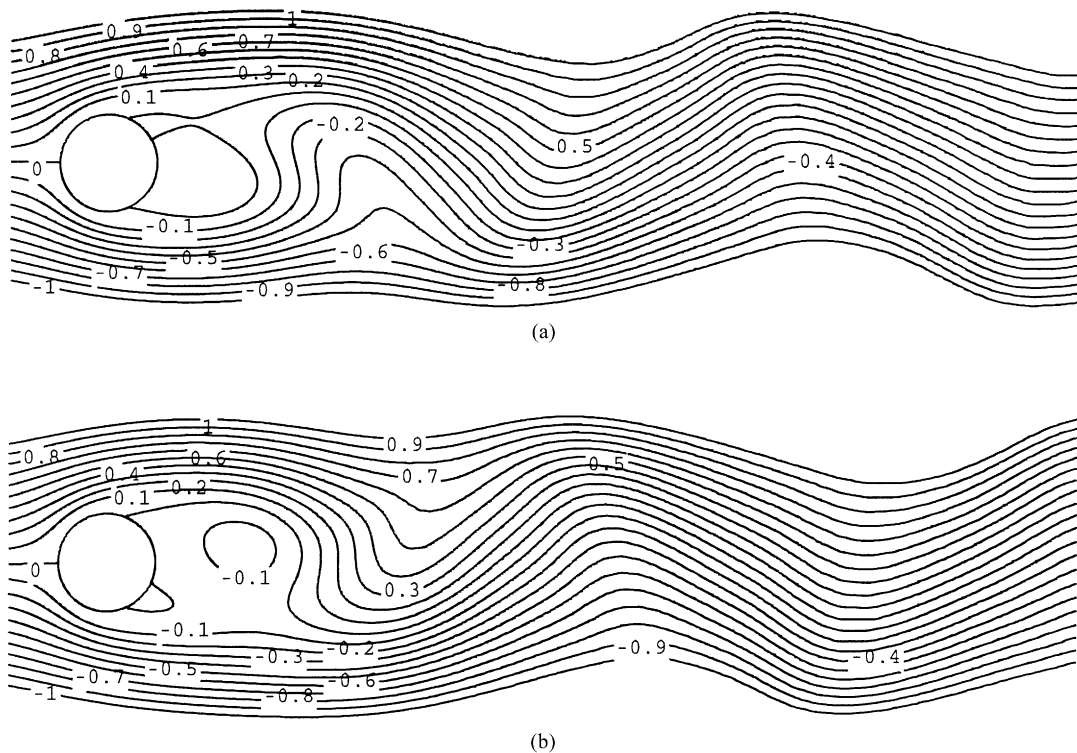


Fig. 11. Instantaneous streamlines around the cylinder at $De = 1$ and $Re = 100$, for: (a) $L^2 = 100$; (b) $L^2 = 1200$.

by a strong damping in lift and velocity fluctuations. The time history of C_D and C_L is shown in Fig. 12; while for $De = 1$ the variation is perfectly sinusoidal, as De is raised the variation becomes more erratic, with the maxima in C_L and C_D varying with time and no longer retaining constant magnitudes. Close inspection of Fig. 12a even shows that C_D at $De = 3$ does not follow any longer a sinusoidal variation, though the period remains approximately constant, without the need to apply fast-Fourier-transform analysis in order to extract the predominant frequency. Streaklines for the three cases of Table 7 are shown in Fig. 13; we note that the same number of massless particles are released per unit time for the three cases, even if the time step used in the computations was smaller for the cases $De = 2$ and 3 (see Table 7). This figure is very elucidative and closely mimics the photos of flow visualisation in

Table 7
Results for varying De at fixed $L^2 = 1200$

De	δt	T_L	St	ΔC_L	$C_{D_{\max}}$	$C_{D_{\min}}$	v'
1	0.025	6.1961	0.1614	0.2662	1.4221	1.4092	0.260
2	0.0125	6.6235	0.1510	0.09594	1.4042	1.3832	0.117
3	0.0125	6.875	0.1454	0.041 ^a	1.413 ^a	1.387 ^a	0.0626

^a Varies.

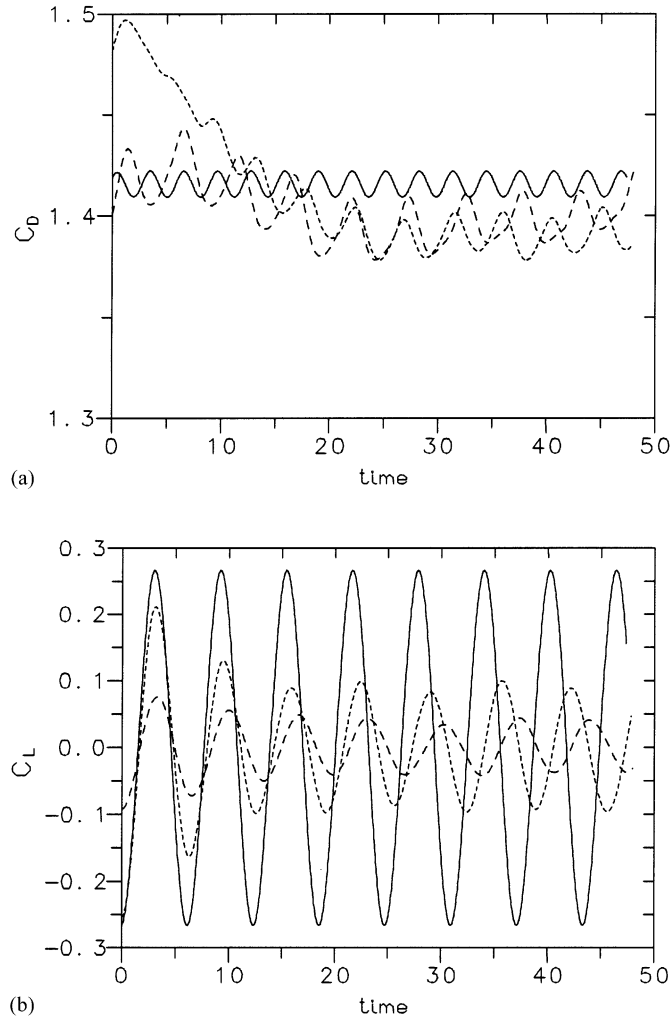


Fig. 12. Effect of elasticity at high L^2 ($L^2 = 1200$; $Re = 100$) on: (a) C_D ; (b) C_L . $De = 1$ (solid line); $De = 2$ (small dash); $De = 3$ (long dash).

[14] (his Fig. 1), [15] (their Fig. 3), and [17] (their Fig. 1). In these experiments, more elastic fluids were obtained by varying the polymer (typically polyethylene oxide) concentration or its molecular weight. The fluid with larger relaxation time in [15] showed an extended transition or formation zone behind the cylinder, where the motion is much slower, exactly as our predictions show in Fig. 13, going from $De = 1$ to 3. The inhibition of vortex formation and increase in the vortex street wavelength are also clearly seen in Fig. 13. Our predictions with high L^2 , and consequently with increased elongation viscosity of the model fluid, are also in agreement with comments made by Cressman et al. [17] who related the effect introduced by the polymer to an “elongational viscosity term” in the Navier–Stokes equations.

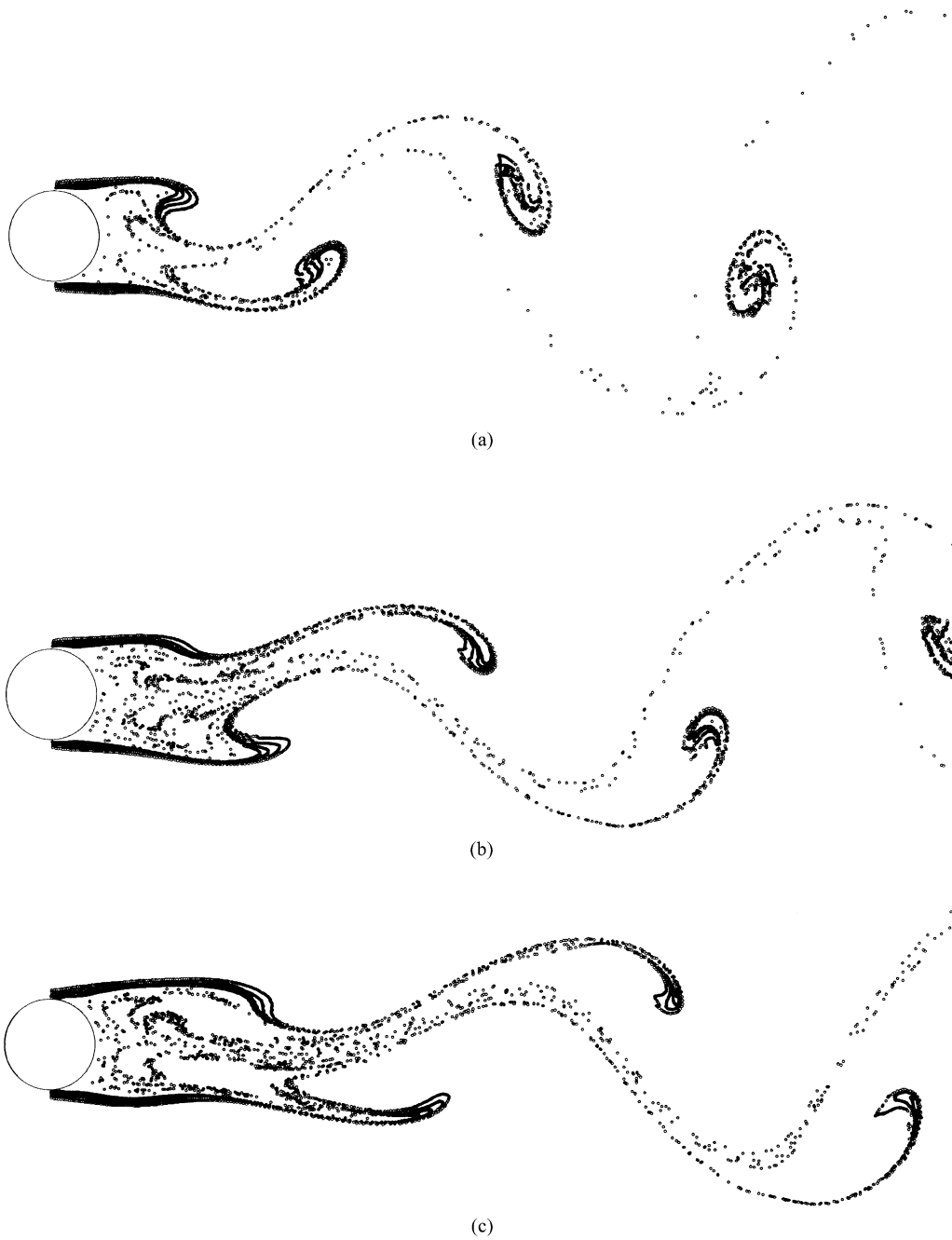


Fig. 13. Streaklines for increasing elasticity at constant $L^2 = 1200$: (a) $De = 1$; (b) $De = 2$; (c) $De = 3$.

5. Conclusions

A finite-volume method for the computation of time-dependent viscoelastic flows is described and is then applied to simulate vortex shedding behind a circular cylinder, for a type of FENE-CR fluid model. The benefits, and in fact the necessity, of employing second-order schemes in time and space are amply demonstrated. In addition, the following conclusions could be drawn from the present results:

1. The formation length behind the cylinder is greatly increased for the elastic fluid. It is about $1.40d$ for the Newtonian fluid ($Re = 100$) and $\approx 2.06d$ for the case at $De = 80$ ($L^2 = 100$). When the extensibility parameter of the viscoelastic model is raised, thus inducing larger elongational viscosities, the formation length is extended even farther (being $\approx 2.4d$ at $De = 2$ and $3.5d$ at $De = 3$, with $L^2 = 1200$). This effect closely mimics the experimental photographs of [14–17] (compare with our Fig. 13).
2. The vortex shedding frequency is attenuated by elasticity, with the calculated rate of decrease of the Strouhal number with the Deborah number, in a decade or more of De , closely matching that found by Usui et al. [18] in their experiments. This point is related to the observed tendency for reduced aspect ratio of the wake (wavelength divided by lateral separation between vortex centres) reported in various experimental works of Cadot and coworkers [14–16].
3. Time-averaged rms fluctuations of the lateral velocity component are also much reduced, when small amounts of a polymer are added to a Newtonian solvent. This fact, experimentally observed by Cressman et al. [17], is also corroborated by the present simulations (v' calculated on the centreline at a distance of $1d$ behind the cylinder is reduced by a factor of 4.2, when De is raised from 1 to 3, with $L^2 = 1200$), and could be related to the phenomenon of drag reduction.

References

- [1] G.H. McKinley, P. Pakdel, A. Öztekin, *J. Non-Newtonian Fluid Mech.* 67 (1996) 19–47.
- [2] B. Yesilata, A. Öztekin, S. Neti, *J. Non-Newtonian Fluid Mech.* 85 (1999) 35–62.
- [3] P.J. Oliveira, F.T. Pinho, *J. Non-Newtonian Fluid Mech.* 88 (1999) 63–88.
- [4] P.J. Oliveira, in: *Proceedings of the 3rd Meeting of Soc. Port. Rheo., Inst. Piaget, 2001*, pp. 97–102.
- [5] O.G. Harlen, J.M. Rallison, P. Szabo, *J. Non-Newtonian Fluid Mech.* 60 (1995) 81–104.
- [6] G.B. Bishko, O.G. Harlen, T.C.B. McLeish, T.M. Nicholson, *J. Non-Newtonian Fluid Mech.* 82 (1999) 255–273.
- [7] P. Wapperom, R. Keunings, V. Legat, *J. Non-Newtonian Fluid Mech.* 91 (2000) 273–295.
- [8] P. Wapperom, R. Keunings, *J. Non-Newtonian Fluid Mech.* 97 (2001) 267–281.
- [9] H.K. Rasmussen, O. Hassager, *J. Non-Newtonian Fluid Mech.* 56 (1995) 65–84.
- [10] H.K. Rasmussen, *J. Non-Newtonian Fluid Mech.* 84 (1999) 217–232.
- [11] G. Monpean, M. Deville, *J. Non-Newtonian Fluid Mech.* 72 (1997) 253–279.
- [12] S.C. Xue, N. Phan-Thien, R.I. Tanner, *J. Non-Newtonian Fluid Mech.* 87 (1999) 337–367.
- [13] P. Wapperom, M.F. Webster, *J. Non-Newtonian Fluid Mech.* 79 (1998) 405–431.
- [14] O. Cadot, *Eur. J. Mech. B Fluids* 20 (2001) 145–153.
- [15] O. Cadot, M. Lebey, *Phys. Fluids* 11 (1999) 494–496.
- [16] O. Cadot, S. Kumar, *J. Fluid Mech.* 416 (2000) 151–172.
- [17] J.R. Cressman, Q. Bailey, W.I. Goldburg, *Phys. Fluids* 13 (2001) 867–871.
- [18] H. Usui, T. Shibata, Y. Sano, *J. Chem. Eng. Jpn.* 13 (1980) 77–79.
- [19] V. Delvaux, M.J. Crochet, *J. Non-Newtonian Fluid Mech.* 37 (1990) 297–315.
- [20] H.H. Hu, D.D. Joseph, *J. Non-Newtonian Fluid Mech.* 37 (1990) 347–377.
- [21] D.F. James, A.J. Acosta, *J. Fluid Mech.* 42 (1970) 269–288.

- [22] R.B. Bird, O. Hassager, R.C. Armstrong, C.F. Curtiss, *Dynamics of Polymer Liquids*, Vol. 2, Wiley, New York, 1977.
- [23] M.D. Chilcott, J.M. Rallison, *J. Non-Newtonian Fluid Mech.* 29 (1988) 381–432.
- [24] P.J. Coates, R.C. Armstrong, R.A. Brown, *J. Non-Newtonian Fluid Mech.* 42 (1992) 141–188.
- [25] J. Remmelgas, L.G. Leal, *J. Non-Newtonian Fluid Mech.* 89 (2000) 231–249.
- [26] B. Purnode, M.J. Crochet, *J. Non-Newtonian Fluid Mech.* 65 (1996) 269–289.
- [27] J. Remmelgas, P. Singh, L.G. Leal, *J. Non-Newtonian Fluid Mech.* 88 (1999) 31–61.
- [28] P.J. Oliveira, F.T. Pinho, G.A. Pinto, *J. Non-Newtonian Fluid Mech.* 79 (1998) 1–43.
- [29] Z. Lilek, S. Muzaferija, M. Perić, V. Seidl, *Numer. Heat Transf. B* 32 (1997) 403–418.
- [30] P.H. Gaskell, A.K.C. Lau, *Int. J. Numer. Meth. Fluids* 8 (1988) 617–641.
- [31] M.A. Alves, P.J. Oliveira, F.T. Pinho, *Int. J. Numer. Meth. Fluids*, 2001, submitted for publication.
- [32] M.A. Alves, F.T. Pinho, P.J. Oliveira, *J. Non-Newtonian Fluid Mech.* 97 (2001) 207–232.
- [33] R.I. Issa, *J. Comp. Phys.* 62 (1986) 40–65.
- [34] I.E. Barton, *Int. J. Numer. Meth. Fluids* 28 (1998) 841–857.
- [35] J.H. Ferziger, M. Perić, *Int. J. Numer. Meth. Fluids* 23 (1996) 1263–1274.
- [36] C.H.K. Williamson, *J. Fluid Mech.* 206 (1989) 579.
- [37] A. Roshko, *NACA Report*, Vol. 1191, 1954.
- [38] D. Kim, H. Choi, *J. Comp. Phys.* 162 (2000) 411–428.